



Gravitational lensing with three-dimensional ray tracing[★]

M. Killadar,^{1,2†} P. D. Lasky,^{3,4†} G. F. Lewis¹ and C. J. Fluke⁴

¹Sydney Institute for Astronomy, School of Physics, The University of Sydney, NSW 2006, Australia

²Dipartimento di Fisica dell’Università di Trieste, Sezione di Astronomia, Via Tiepolo 11, I-34131 Trieste, Italy

³Theoretical Astrophysics, Eberhard Karls University of Tübingen, Tübingen 72076, Germany

⁴Centre for Astrophysics and Supercomputing, Swinburne University of Technology, PO Box 218, Hawthorn, VIC 3122, Australia

Accepted 2011 October 15. Received 2011 October 4

ABSTRACT

High-redshift sources suffer from magnification or demagnification due to weak gravitational lensing by large-scale structure. One consequence of this is that the distance–redshift relation, in wide use for cosmological tests, suffers lensing-induced scatter which can be quantified by the magnification probability distribution. Predicting this distribution generally requires a method for ray tracing through cosmological N -body simulations. However, standard methods tend to apply the multiple-thin-lens approximation. In an effort to quantify the accuracy of these methods, we develop an innovative code that performs ray tracing without the use of this approximation. The efficiency and accuracy of this computationally challenging approach can be improved by careful choices of numerical parameters; therefore, the results are analysed for the behaviour of the ray-tracing code in the vicinity of Schwarzschild and Navarro–Frenk–White lenses. Preliminary comparisons are drawn with the multiple-lens-plane ray-bundle method in the context of cosmological mass distributions for a source redshift of $z_s = 0.5$.

Key words: gravitational lensing: weak – methods: numerical – cosmology: theory – large scale structure of Universe.

1 INTRODUCTION

Weak gravitational lensing of distant galaxies by large-scale structure leads to the distortion of their images. In an inhomogeneous universe, each line of sight probes a slightly different integrated mass and is sheared differently; overdense regions result in magnification and underdense regions cause demagnification. The result is that for a given redshift z , a source is magnified (or demagnified) by some amount μ , *relative to the case of a perfectly homogeneous universe at all scales*. This magnification has an associated probability distribution that reflects the existence of structure on a range of scales.

Large surveys for galaxies, quasars and supernovae suffer a two-fold *magnification bias* as a result of the same phenomenon. When a source is magnified, its total surface area on the sky is increased; consequently, for a given area of sky observed, the region of the source plane being sampled is decreased. On the other hand, magnification will push otherwise too-faint sources above the observational threshold in flux-limited surveys (Canizares 1981; Turner,

Ostriker & Gott 1984); this is particularly important for optically selected quasar surveys (Peacock 1982; Bartelmann & Loeb 1996; Wyithe et al. 2011). Together, these two effects have counteracting influences on source counts, but generally do not cancel each other out. Additionally, for sources that are demagnified, the effect is reversed; indeed, the majority of sources are demagnified relative to the case of a perfectly homogeneous universe. The net effect on source counts, observed luminosity functions, source redshift distributions and any resulting bias depends on selection procedures, intrinsic source properties and the probabilistic lensing effect (Dyer & Roeder 1974; Peacock 1982; Le Brun et al. 2000). The intrinsic source luminosity function and magnification probability distribution function (hereinafter μ PDF) are unknowns; the former is generally modelled as a Schechter function (Schechter 1976). An appropriate model for the latter – which may be produced by ray tracing through N -body simulations – is the subject of this study (see Section 2.1). Hamana, Martel & Futamase (2000) and Jain & Lima (2011) have demonstrated that a power-law tail in the μ PDF significantly changes the shape of the bright end of the luminosity function and generates a considerable magnification bias for high-redshift sources.

Gravitational lensing causes magnification or demagnification of Type Ia supernovae (SNeIa), resulting in a scatter in the inferred distance–redshift distribution, particularly for high-redshift sources (Jönsson et al. 2008). The lensing-induced scatter introduces a bias and uncertainty in the inferred values of the matter density

[★]Research undertaken as part of the Commonwealth Cosmology Initiative (CCI: www.thecci.org), an international collaboration supported by the Australian Research Council (ARC).

†E-mail: killedar@oats.inaf.it (MK); lasky@tat.physik.uni-tuebingen.de (PDL)

parameter, $\Omega_{M,0}$, the deceleration parameter, q_0 , and the dark energy equation of state, w (Wambsganss et al. 1997; Astier et al. 2006; Jönsson et al. 2008). For example, in the case of the $z = 1.7$ supernova SN1997ff, the estimated magnification would easily bridge the gap between evidence supporting a Λ cold dark matter (Λ CDM) universe and that supporting an empty universe. The lensing effect can be ‘averaged out’, for supernova samples, by combining measurements from a sufficiently large number of sources at similar redshifts (Holz & Wald 1998; Holz & Linder 2005). However, a similar scatter will be induced by lensing in the Hubble diagram drawn from measurements of gravitational waves, the so-called standard sirens (Marković 1993; Holz & Hughes 2005; Jönsson, Goobar & Mörtzell 2007). Efforts are now underway to provide an appropriate method for correcting the observed brightnesses of individual objects for magnification (e.g. Gunnarsson et al. 2006; Jönsson, Mörtzell & Sollerman 2009; Shapiro et al. 2010; Hilbert, Gair & King 2011). By accounting for the non-Gaussian shape of the μ PDF, one is best able to correct for the effects of lensing statistically (Hirata, Holz & Cutler 2010; Shang & Haiman 2011).

There are many approaches to determine the μ PDF for a given cosmological model. The optical scalar equations (Sachs 1961), which describe the evolution of the cross-section of a small beam of light, have been applied to various mass distributions leading to useful redshift–distance relations in the limiting case when the line of sight is far away for inhomogeneities (Kantowski 1969; Dyer & Roeder 1974; Dyer 1977). The equations have also been applied to an infinitesimal beam transported through a generalized inhomogeneous universe that, on average, satisfies the Friedmann–Lemaître–Robertson–Walker (FLRW) geometry in order to re-derive the maximal angular diameter distance (Seitz, Schneider & Ehlers 1994). A simple integration of the optical scalar equations would be possible in the case of a known metric, but that is the crux of the problem – the local metric for an inhomogeneous universe has no general (analytic) solution. Crude model universes incorporate inhomogeneities and describe their effects on light propagation (e.g. Dyer & Roeder 1972; Linder 1988; Futamase & Sasaki 1989). However, when the cosmological structure being probed is highly non-linear and lines of sight have small impact parameters, studying light deflection requires the use of numerical techniques.

The non-linear and hierarchical growth of the large-scale structure is generally modelled by cosmological N -body simulations, with the propagation of light and its subsequent lensing computed by ray tracing through these simulations. Some methods consider only one dominant lens in each line of sight; the lensing object is thin compared to the distances between the observer, lens and source – this is known as the thin-lens approximation. However, multiple lenses coincident along the line of sight may be responsible for a lensing event (Wambsganss, Bode & Ostriker 2005; Das & Ostriker 2006). The existence of multiple-lens plane also accounts for the finding of Premadi et al. (2001) that the magnification probability, $P(\mu > 1)$, is mostly independent of the parameter that quantifies the normalization of the matter power spectrum, σ_8 . Rauch et al. (1992) identified a feature of the μ PDF: a ‘bump’ that was only evident when considering two-dimensional projections of matter; they speculated that changes to the caustic structure resulting from the projection were somewhat responsible. The presence of this caustic-induced bump was confirmed by Lee et al. (1997), who derived a semi-analytic expression for this feature in the limit of low optical depth. Therefore, in the context of cosmological structure, the thin-lens approximation should be replaced, at the very least, by the multiple-lens-plane approach (see Section 3.1), where large volumes of matter are projected on to a series

of lens planes (Blandford & Narayan 1986; Kovner 1987). The ray-shooting method, developed by Kayser, Refsdal & Stabell (1986), Schneider & Weiss (1988), Wambsganss (1990) and Wambsganss, Cen & Ostriker (1998), embodies this approach. Subsequent introduction of tree methods to measure the deflection angle at each lens plane has produced efficient algorithms. Early ray-shooting techniques were applied to a random distribution of point masses, which therefore did not incorporate the intricacies of clustering properties within various cosmological models (Schneider & Weiss 1988; Paczynski & Wambsganss 1989; Lee & Paczynski 1990). Later studies coupled the multiple-lens-plane approach with mass distributions taken from N -body simulations to study the effect and magnitude of gravitational lensing (e.g. Jaroszynski et al. 1990).

While it is tempting to continue using the previous methods because of their simplicity, one must first quantify the effect that the various approximations have on the resulting predictions. Galaxy redshift surveys such as the CfA survey (Davis et al. 1982) and the 2dFGRS (Cole et al. 2005) have revealed that elongated structures exist in the form of filaments, which stretch across large voids between galaxy clusters. These are also evident in cosmological simulations. If such filaments are projected on to lens planes, the resulting magnification would be overestimated. Though earlier computational limitations, such as memory and processing, warranted the need for these simplifications, we are now entering an era where more accurate methods are within our reach.

Only a few studies have numerically integrated the null geodesic equations from the observer to source. The earliest of these studies assumed metrics that were approximated via a simplified model for inhomogeneities and derived distance–redshift relations which were compared to the Dyer–Roeder approximations (Futamase & Sasaki 1989; Watanabe & Tomita 1990). Kasai, Futamase & Takahara (1990) drew attention to the spread in angular diameter distances, given a small enough beam size and the fact that the average value was consistently lower than the solution for a homogeneous universe. Tomita (1998) numerically integrated the null geodesic equations through N -body simulations, albeit at low resolution, finding that various cosmologies exhibited differences in angular diameter distances. Couchman, Barber & Thomas (1999) developed a three-dimensional algorithm for modelling weak gravitational lensing; comparing the two-dimensional shear with three-dimensional shear, they found that the projection of structure on $100 h^{-1}$ Mpc scales led to errors of up to 9 per cent depending on the redshift of the lens box. Vale & White (2003) performed three-dimensional ray tracing by computing the deflection angle for rays many times along their path, advancing them in step-sizes of L_{box}/N_g along the line of sight. In their study, they used a relatively small number of grid points along the line of sight, $N_g = 32$, such that the step-size was approximately $10 h^{-1}$ Mpc, but boxes of half that size were used for numerical tests. They found that their convergence maps were unchanged to 0.1 per cent. White & Hu (2000) ran simulations of structure formation while simultaneously propagating photons through the said simulations; they were able to produce convergence fields from the light rays they follow.

What has been missing thus far is a one-to-one comparison of results that take a multiple-lens approach and a direct numerical integration of the null geodesic equations; this comparison is carried out in this work. In Section 2, the basic theory and notation of gravitational lensing and the relevant statistics are presented. We introduce the method of numerically integrating the null geodesic equations in Section 3 with specific reference to its multiple-lens-plane counterpart; in Section 4, we establish the accuracy and limitations of the method. We describe the simulations used for modelling the

cosmological mass distribution and compare statistical predictions determined by the two methods discussed in Section 5. Finally, a summary of our findings is presented in Section 6.

2 GRAVITATIONAL LENSING

Here, we introduce the conventional notation for the components that describe the effect of gravitational lensing on the shape of a beam to first order. Each background source experiences lensing in the form of convergence, κ , and shear, γ . Convergence is the isotropic Ricci focusing of a beam due to enclosed matter, while shear is the tidal stretching of the beam along a particular axis due to asymmetric matter distribution; together, they serve to increase the area of the source on the sky, resulting in its magnification, due to the conservation of surface brightness. The two-dimensional effective lensing potential, ψ_{2D} , is given by

$$\psi_{2D}(\mathbf{x}) = \frac{1}{\pi} \int_{\mathbb{R}^2} d^2x' \kappa(\mathbf{x}') \ln |\mathbf{x} - \mathbf{x}'|. \quad (1)$$

Here \mathbf{x} is a dimensionless vector formed by scaling the image position, ξ :

$$\mathbf{x} = \frac{\xi}{\xi_0}. \quad (2)$$

For a single thin lens, κ is equivalent to the scaled surface density of the lens, and is related to the gravitational potential via the Poisson equation

$$\frac{1}{2} \nabla^2 \psi_{2D} = \kappa = \frac{\Sigma}{\Sigma_{\text{crit}}}, \quad (3)$$

where the critical surface density for gravitational lensing is given by

$$\Sigma_{\text{crit}} = \frac{c^2}{4\pi G} \frac{D_s}{D_d D_{ds}}. \quad (4)$$

Thus, lensing is characterized by D_s , D_d and D_{ds} , the angular diameter distances from the observer to the source, from the observer to the (thin) lens, and from the lens to the source, respectively. Total shear can be written in complex notation; its dependency on the two orthogonal components is given by

$$\gamma = \gamma_1 + i\gamma_2, \quad (5)$$

where the two components are linearly related to the second derivatives of the (projected) gravitational potential along two orthogonal directions by

$$\gamma_1 = \frac{1}{2}(\psi_{,11} - \psi_{,22}) \quad \text{and} \quad \gamma_2 = \psi_{,12}, \quad (6)$$

where the indices after the comma denote partial differentiation and we temporarily drop the subscript 2D for clarity. The deformation of the beam is described as a mapping from the source plane to the image (observed) plane. The Jacobian, \mathbf{A} , of the lens mapping is a real and symmetric 2×2 matrix given by

$$\mathbf{A} \equiv \begin{pmatrix} 1 - \kappa - \gamma_1 & -\gamma_2 \\ -\gamma_2 & 1 - \kappa + \gamma_1 \end{pmatrix}. \quad (7)$$

The flux magnification of an image is given by the inverse of the determinant of the Jacobian, so

$$\mu = \frac{1}{(1 - \kappa)^2 - |\gamma|^2}. \quad (8)$$

One may now consider the effect of lensing on the apparent position of the image of the source of light. The scaled deflection angle is

the gradient of the lensing potential:

$$\boldsymbol{\alpha}_{2D} = \nabla \psi_{2D} \quad (9)$$

$$= \frac{1}{\pi} \int_{\mathbb{R}^2} d^2x' \kappa(\mathbf{x}') \frac{\mathbf{x} - \mathbf{x}'}{|\mathbf{x} - \mathbf{x}'|^2}. \quad (10)$$

The gravitational lens equation is therefore given by

$$\boldsymbol{\beta} = \boldsymbol{\theta} - \boldsymbol{\alpha}_{2D}(\boldsymbol{\theta}), \quad (11)$$

where $\boldsymbol{\beta}$ is the angular source position and $\boldsymbol{\theta}$ is the angular position of the image on the sky. The deflection angle, $\hat{\boldsymbol{\alpha}}$, is related to its scaled counterpart by

$$\hat{\boldsymbol{\alpha}}_{2D} = \frac{\xi_0 D_s}{D_d D_{ds}} \boldsymbol{\alpha}_{2D}. \quad (12)$$

2.1 The magnification probability distribution

The probability that a source at redshift z would be magnified by an amount within the interval $[\mu, \mu + d\mu]$ is $p(\mu, z)d\mu$. It satisfies

$$\int_0^\infty p(\mu, z) d\mu = 1. \quad (13)$$

When the μ PDF is convolved with intrinsic luminosity distributions for standard candles, the result describes the observed spread in magnitudes. Flux conservation (Weinberg 1976) demands that $p(\mu, z)$ satisfies

$$\langle \mu \rangle \equiv \int_0^\infty \mu p(\mu, z) d\mu = 1. \quad (14)$$

There exists a minimum magnification, indeed a minimum convergence, which corresponds to a line of sight that encounters no matter between the observer and source; this is also referred to as an empty beam (Dyer & Roeder 1972). The distribution function peaks at values below $\mu = 1$ and is highly skewed towards high magnifications (Hamana et al. 2000). For low-redshift sources and/or small lensing optical depths, the high magnification tail will exhibit a power-law trend $p(\mu) \propto \mu^{-3}$, which results in a formally divergent standard deviation (Vietri & Ostriker 1983). This result was originally derived analytically for a random distribution of compact lenses where only one lens dominates; however, Pei (1993) have noted that for higher optical depths, the slope of tail may become shallower. The precise shape of the distribution depends on the assumed density profile of the lenses (Yoo et al. 2008). The spread in this distribution increases with source redshift (Babul & Lee 1991). For a fixed source redshift, the shape of the distribution, particularly for low magnifications, depends mostly on the cosmological parameter σ_8 and the vacuum density parameter, $\Omega_{\Lambda,0}$ (Premadi et al. 2001). The high-magnification region suffers from low number statistics and since it represents the effects of strong lensing, it cannot be probed by ray-bundle methods (RBMs), which we now discuss.

3 RAY TRACING

3.1 Multiple-lens-plane methods

The multiple-lens-plane method requires the total three-dimensional mass distribution to be sliced up into contiguous boxes; each box is then projected on to a plane perpendicular to the line of sight, usually placed at the centre of the box. In backward-ray-tracing methods, light rays are propagated from the observer to the

source with deflections *only* occurring in successive lens planes. The deflection at a given plane is the result of matter within that plane only. The formalism for the resulting deflection can be written in terms of the multiple-lens-plane equation derived and developed by Blandford & Narayan (1986), Schneider & Weiss (1988) and Jaroszynski et al. (1990); the source position, η , after deflection by N lens planes is

$$\eta = \frac{D_{\text{os}}}{D_{\text{o1}}} \xi_1 - \sum_{i=1}^N D_{is} \hat{\alpha}_i(\xi_i), \quad (15)$$

where ξ_i is the position of the ray in the i th lens plane; ξ_1 therefore is the position of the image. D_{os} , D_{o1} and D_{is} are the angular diameter distances from the observer to the source, from the observer to the first lens plane, and from the i th lens to the source, respectively. Note that high-density regions in a plane may not necessarily be dense in real space.

One approach to studying the statistics of gravitational lensing is the RBM, developed by Fluke, Webster & Mortlock (1999), and also see Fluke (1999). Here, the multiple-lens-plane method is used to propagate light rays from the observer to a given source plane. Instead of employing a grid-based technique for calculating magnifications across the source plane, the approach favoured by other backward-ray-tracing codes (e.g. Jain, Seljak & White 2000; Premadi et al. 2001), the RBM models each individual line of sight as an ‘infinitesimal bundle’ of light rays around a central ray and follows this bundle back to the source plane. An initially circular image is distorted by the time it reaches the source plane as a result of convergence and shear. These quantities can be determined for this specific line of sight as the image–source association is maintained. In the RBM, N rays in a regular polygon represent a circular image and their positions at the source plane are fitted with an ellipse; the Jacobian matrix (equation 7) is determined for each bundle and solved to determine μ , κ and γ .

The ray-tracing method presented in this work uses the RBM design of a ray bundle with eight rays, but does away with the multiple-lens-plane treatment of the lensing mass. Instead, the evolution of the cross-section of the bundle is determined by integrating the null geodesic using a numerical gravitational potential obtained from N -body simulations.

3.2 The weak-field metric

The FLRW geometry describes a universe that is homogeneous on all scales. The FLRW line element for a flat geometry is

$$ds^2 = -dt^2 + R^2(t) [d\chi^2 + \chi^2 (d\theta^2 + \sin^2\theta d\phi^2)], \quad (16)$$

where χ , θ and ϕ are comoving coordinates. The metric allows an evolving scalefactor, $R(t)$. From here onwards, we quantify the scalefactor relative to its current value, that is, at $t = 0$,

$$a(t) \equiv \frac{R(t)}{R(0)}. \quad (17)$$

We assume that the inhomogeneities present in large-scale structure are small enough to be represented as a perturbation to the background FLRW metric, and do not falsify the large-scale predictions made under the FLRW geometry. The resulting line element is

$$ds^2 = -[1 + 2\psi(t, \mathbf{x})] dt^2 + a^2(t) [1 - 2\psi(t, \mathbf{x})] d\mathbf{x}^2. \quad (18)$$

The weak-field metric is applicable where $\psi(t, \mathbf{x}) \ll a(t)$. The gravitational potential, which is defined with respect to the local

perturbation from a smooth background (see Section 3.3), can be decoupled,

$$\psi(t, \mathbf{x}) = \frac{\phi(\mathbf{x})}{a(t)}, \quad (19)$$

such that ψ is defined in physical units and ϕ in comoving. The Christoffel symbols for this metric, presented in Appendix A, are dependent not only on the gradients of the gravitational potential ϕ , but also on ϕ *itself*, which is defined based on the mass perturbation from a smooth background. The geodesic equations (see equation 27 below), which are the second-order differential equations for the four coordinates, are then constructed.

3.3 The gravitational potential

The perturbation field

$$\delta(t, \mathbf{x}) \equiv \frac{\rho(t, \mathbf{x}) - \bar{\rho}(t)}{\bar{\rho}(t)} \quad (20)$$

relates the local density, $\rho(t, \mathbf{x})$, to the mean matter density, $\bar{\rho}(t)$, the latter of which is given by

$$\bar{\rho}(t) = \Omega_M \rho_c(t). \quad (21)$$

The critical density, $\rho_c(t)$, is given by

$$\rho_c(t) = \frac{3H^2(t)}{8\pi G}, \quad (22)$$

where $H(t)$ is the Hubble parameter:

$$H(t) = \frac{\dot{R}(t)}{R(t)}. \quad (23)$$

The perturbation is related to the gravitational potential $\psi(t, \mathbf{x})$ by

$$\psi(t, \mathbf{x}) = -\frac{4\pi G}{c^2} \bar{\rho}(t) \int_{\mathbb{R}^3} d\mathbf{x}'^3 \frac{\delta(t, \mathbf{x}')}{|\mathbf{x} - \mathbf{x}'|}. \quad (24)$$

The derivatives of the gravitational potential are then

$$\frac{d\psi(t, \mathbf{x})}{d\mathbf{x}^j} = \frac{4\pi G}{c^2} \bar{\rho}(t) \int_{\mathbb{R}^3} d\mathbf{x}'^3 \delta(t, \mathbf{x}') \frac{\mathbf{x} - \mathbf{x}'}{|\mathbf{x} - \mathbf{x}'|^3}. \quad (25)$$

One can relate the numerically determined ϕ to the gravitational potential via equation (19) and derivatives in a similar fashion:

$$\frac{d\psi(t, \mathbf{x})}{d\mathbf{x}^j} = \frac{1}{a(t)} \frac{d\phi(\mathbf{x})}{d\mathbf{x}^j}. \quad (26)$$

Constructing the grids that represent the perturbation field and its derivative requires a few steps. First, if the lensing mass is discretized into particles, then the mass within a cube of comoving side length L_{box} is assigned to the nodes of a regular grid using the Cloud-in-Cell (CIC) algorithm (Hockney & Eastwood 1988) in three dimensions; the mean matter density is then subtracted off. A fast Fourier transform (FFT) is applied to convolve the mass distribution with the appropriate kernels to determine the gravitational field and its derivatives according to equations (24) and (25), using the popular software package FFTW (Fastest Fourier Transform in the West).¹ Depending on the lens, a periodic mass distribution may be implied, or not. If not, then the density grid is zero-padded before performing the FFT convolution. At many stages during the integration, the local values of the field and its derivatives need to be evaluated, so an interpolation scheme was written for this purpose; it is described in detail in Appendix B.

¹ <http://www.fftw.org/>

There are two numerically intensive parts of the ray-tracing method: the first is the set of FFTs required to calculate the gravitational potential and its derivatives at every grid point on a three-dimensional mesh; the second is the interpolation required at each time-step to determine the values of the same quantities at the exact position of the light ray.

Note also that the Fourier-grid resolution sets a lower limit to the scale of structure probed, as the mass is smoothed over this grid scale. This is assuming that this scale is reasonably larger than the softening length employed in the N -body simulations used to model the cosmological mass distribution.

3.4 Three-dimensional ray tracing

Our approach is based on avoiding the approximation of the multiple-lens-plane method. Instead, the path of a photon is numerically integrated from the geodesic equation

$$\frac{d^2x^\alpha}{d\lambda^2} = -\Gamma_{\beta\gamma}^\alpha \frac{dx^\beta}{d\lambda} \frac{dx^\gamma}{d\lambda}. \quad (27)$$

Here $\Gamma_{\beta\gamma}^\alpha$ denotes the Christoffel symbols associated with the metric, x^i represents any of the four coordinates specified by the superscript i , and λ is the affine parameter.

The four second-order differential equations are reduced to eight coupled first-order differential equations, which are integrated with the affine parameter λ as the dependent variable. A classical fourth-order Runge–Kutta integration scheme with fixed step-size was written and used to perform the integration. The subtlety is that it is the x^3 -coordinate, rather than the affine parameter, that determines the boundaries of the integration. The exact evolution of the affine parameter will be different for each ray bundle, and is not known in advance. Therefore, the integral is repeated in small steps of λ , $\Delta\lambda_{RK}$, until x^3 reaches the value required at the source plane $D_C(z_s)$. The step-size is chosen such that the estimated resultant step in x^3 is a fixed fraction, f_{RK} , of the Fourier-grid resolution:

$$\Delta\lambda_{RK} = \frac{f_{RK} L_{\text{box}}}{n_{\text{FFT}} \dot{x}_0^3}, \quad (28)$$

where the overdot denotes the derivative with respect to λ , the extra subscript 0 denotes values at $t = 0$, and n_{FFT} denotes the number of points along one side of the Fourier grid (see Section 3.3). If the ray overshoots the source plane, a simple linear interpolation, using the current and previous positions, is used to find the final source position. The use of a fixed step-size is deemed appropriate as the values of the Christoffel symbols are interpolated from gridded values, as described in Section 3.3. There would be little information gain from step-sizes much smaller than the grid resolution. Nevertheless, the effect of the choice of step-size is analysed, along with other numerical parameters, with results presented in Sections 4.1 and 4.2.

3.5 Evolution of the scalefactor

For certain cosmologies, the Friedmann equations can be solved to find the specific time dependence of the scalefactor; for a spatially flat, radiation-free Lemaitre model ($\Omega_k = 0$, $\Omega_M + \Omega_\Lambda = 1$), with $\Omega_\Lambda > 0$, this dependence is given by

$$a(t) = \left\{ \frac{\Omega_{M,0}}{\Omega_{\Lambda,0}} \sinh^2 \left[\frac{3}{2} \sqrt{\Omega_{\Lambda,0}} H_0 (t_0 - t) \right] \right\}^{1/3}, \quad (29)$$

where t_0 is given by

$$t_0 = \frac{2}{3H_0 \sqrt{\Omega_{\Lambda,0}}} \sinh^{-1} \frac{\Omega_{\Lambda,0}}{\Omega_{M,0}}. \quad (30)$$

Equations (29) and (30) were derived from equation (15.36) in Hobson, Efstathiou & Lasenby (2006), the solution for a spatially flat, matter-only Lemaitre model, but with t used to denote *look-back time* instead.

As the photon traverses a single lens box, the scalefactor will evolve (i.e. decrease) although the comoving scale of the structure does not change appreciably over this time-scale. The value of the scalefactor is required to evaluate the Christoffel symbols, so we evolve the look-back time for the photon as well as the spatial coordinates and use this to determine the scalefactor at each position throughout the box.

4 COMPACT LENS MODELS

Here, we present results of ray tracing in the vicinity of simple lenses. Both the lens models used are fairly compact, and so the thin-lens approximation applied in the analytic solution is suitable. The analytic solutions should be read as magnification for the *image* at that location, rather than the total magnification of the source. This is an important distinction. The ray-bundle approach only follows the congruence corresponding to a single image, and therefore cannot account for the total magnification of multiply imaged sources; this is one of the reasons why it should not be used to model strong lensing. Yet for these simple lenses, we are still able to test our results against the known magnification of a single image for an otherwise strongly lensed source.

4.1 Schwarzschild lenses

The Schwarzschild lens, a singular density point, is the simplest lens one may study. The analytic solution for the magnification for an image at any location is well known and is presented in Appendix C. Since the gravitational potential here is equivalent to a kernel (see equation 24) multiplied by the mass of the lens, we directly compute the gravitational field at each grid point, before performing the ray tracing. The solution for this lens is scale-invariant, so by increasing the mass of the lens, we may essentially increase the resolution of the grid, and make it possible to study the behaviour of ray bundles that pass near (or inside) the Einstein radius. In cosmological simulations, the RBM explicitly avoids this as the images near the Einstein ring are part of multiple sets of images, and the images inside the ring are the demagnified images that contribute only a small portion of the magnification of the associated source. However, for testing purposes, we allow lines of sight that approach the Einstein radius, since the analytic solution is known for each individual image. In the fiducial test case, the Schwarzschild lens has a mass of $10^{15} M_\odot$. It is placed at a redshift of $z_L = 0.35$, giving it an Einstein radius of 65.6 arcsec for a source redshift of $z_s = 0.8$, which corresponds to ~ 12 mesh points on the 256^3 Fourier grid.

The ray-tracing code developed here is able to reproduce the desired lensing distortion very well. The left-hand panels of Fig. 1 show that even high-magnification events, which occur when the image is near the Einstein radius, are recovered by the numerical method.

The numerical error, shown in the right-hand panels, increases for images that are closer to this radius where the higher order lensing effects, like flexion, are expected to play a role, and an eight-ray bundle has limited application regardless of the choices of other numerical parameters. Note that in each of the tests shown in Figs 1–4, the results break down in the very centre of the lens. We choose 3 per cent as an error threshold to mark the sharp upturn in the average error at small impact parameters. The error surpasses

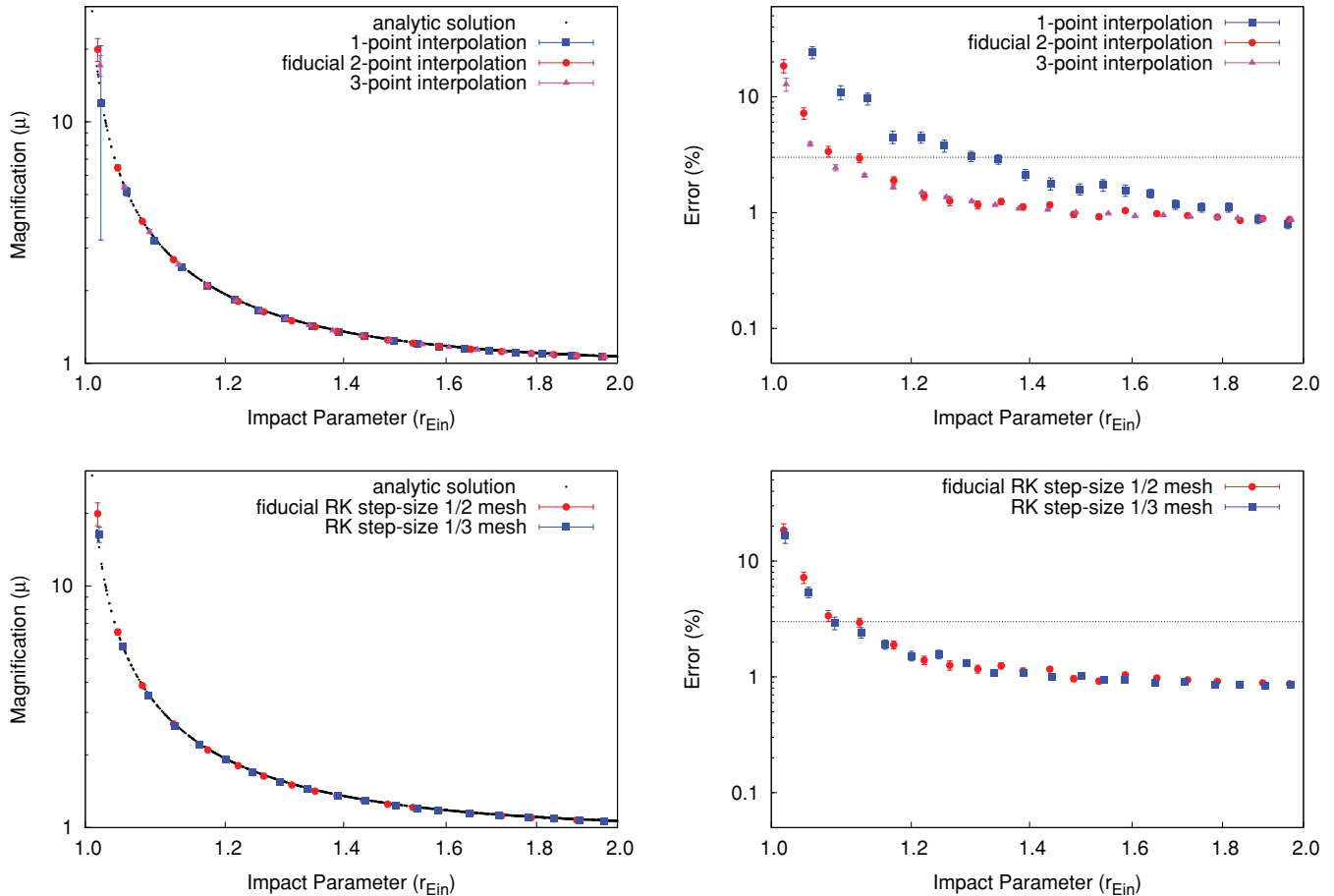


Figure 1. The radial dependence of magnification (μ ; left-hand panels) and the percentage error in the numerical magnification ($\Delta\mu/\mu$; right-hand panels) when ray tracing past a Schwarzschild lens. Different values of numerical parameters are compared. Top panels: results are shown for the number of points used to interpolate the local potential field and its derivatives: $n_{\text{int}} = 1$ (blue squares); $n_{\text{int}} = 2$ (red circles); and $n_{\text{int}} = 3$ (pink triangles). Bottom panels: results are shown for the Runge–Kutta step-size, that is, half the Fourier-grid resolution (red circles) or one-third the grid resolution (blue squares). In each case, 10^3 lines of sight have been distributed and binned uniformly with $\log(r/r_{\text{vir}})$ and 1σ error bars are shown. The analytic solution (black dots) at each impact parameter sampled is included in the left-hand panels. In the right-hand panels, the dotted horizontal line marks the 3 per cent error threshold.

3 per cent when the impact parameter is smaller than a limiting radius, hereinafter referred to as the ‘minimum reliable radius’, or MRR. The MRR can be used as a measure of numerical accuracy and the effect of numerical parameters. For example, the top panels of Fig. 1 show the result of decreasing the number of interpolation points so that just one Fourier-grid node *on either side* of the current position is used to find the local values of the gravitational field and its derivatives. In this case, the MRR expands out to a larger impact parameter where only low-magnification regions ($\mu \lesssim 1.5$) are recovered with <3 per cent accuracy. However, once the number of interpolation points is increased beyond this, this parameter has little influence on the accuracy of the results. Likewise, in the bottom panels of Fig. 1, we show the result of reducing the Runge–Kutta step-size; a step that is approximately half the size of the Fourier-grid resolution ($f_{\text{RK}} = 0.5$) is sufficient for accuracy at moderate magnifications ($1.5 \lesssim \mu \lesssim 6$). Decreasing this parameter has negligible effect on the results.

4.2 NFW lenses

Various studies of cosmological simulations (Navarro, Frenk & White 1995) have found that dark matter haloes on galactic and cluster scales have mass distributions that are well described by a

Navarro–Frenk–White (NFW) profile:

$$\rho(r) = \frac{\delta_c \rho_c}{(r/r_s)(1+r/r_s)^2}. \quad (31)$$

Here, ρ_c is the critical density (see equation 22) *at the halo redshift*; r_{200} is the radius within which the mean density of the halo is $200\rho_c$; $r_s = r_{200}/c_\Delta$ is the characteristic scale radius, which marks the transition in the slope of the profile; and c_Δ is the dimensionless concentration parameter. Finally, the characteristic overdensity is given by

$$\delta_c = \frac{200}{3} \frac{c_\Delta^3}{\ln(1+c_\Delta) - c_\Delta/(1+c_\Delta)}. \quad (32)$$

We use this profile to compare how the multiple-lens-plane approach and the three-dimensional approach model lensing around galaxies and cluster haloes, where most of the high-magnification events will occur.

Lenses with the NFW profile were modelled by discretizing the mass contained in one virial radius into a number of particles of equal mass and constructing a fake simulation output in the GADGET format. The numerically determined gravitational potential is therefore *not* equivalent to the analytic solution, but suffers from discretization effects just as a simulated halo would. The spherically symmetric lens is divided into a fixed number of radial bins

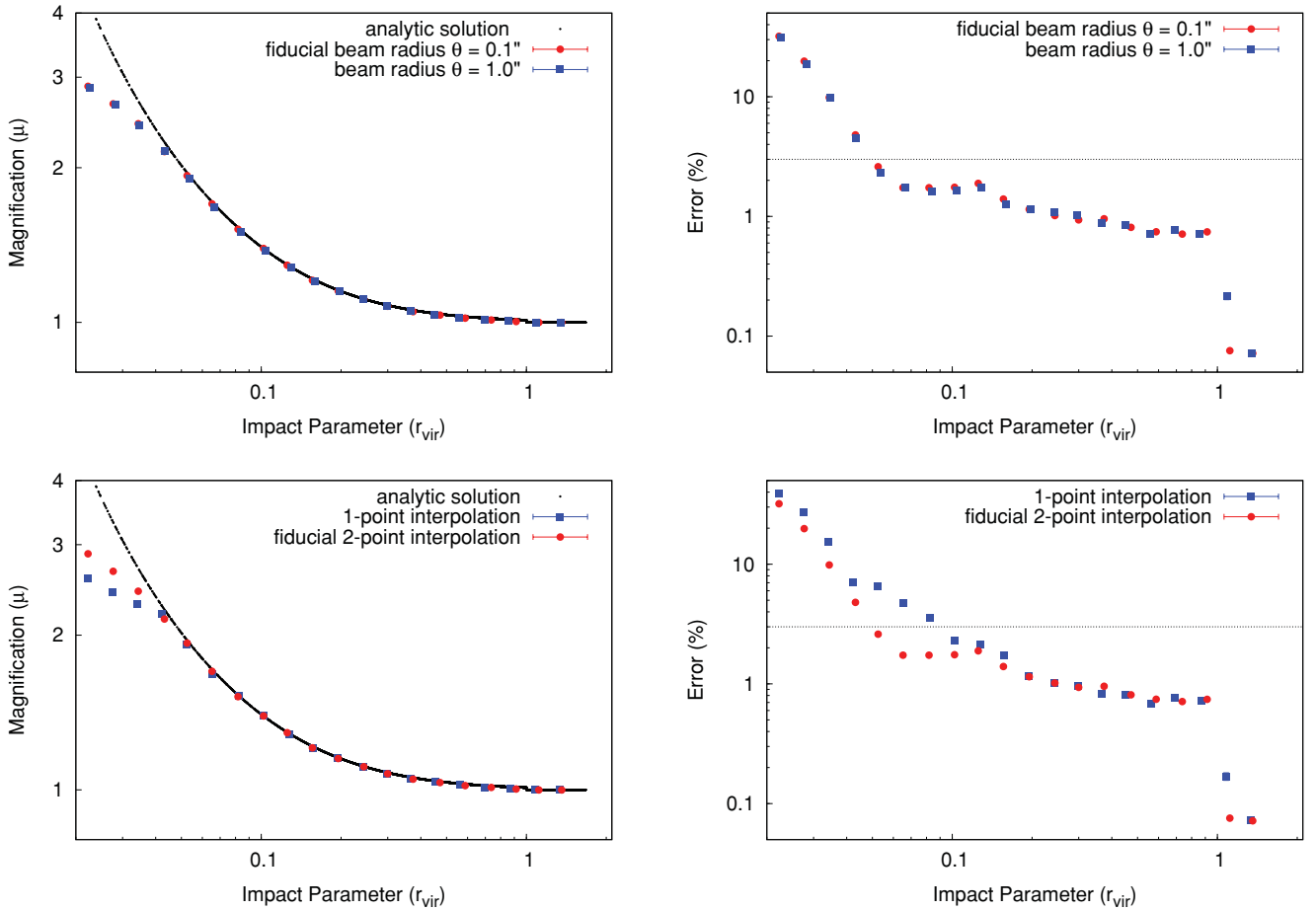


Figure 2. The radial dependence of magnification (μ ; left-hand panels) and the percentage error in the numerical magnification ($\Delta\mu/\mu$; right-hand panels) when ray tracing through a discretized NFW lens. Different values of numerical parameters are compared. Top panels: radius of the ray bundle/image: $\theta = 0.1$ arcsec (red circles); and $\theta = 1$ arcsec (blue squares). Bottom panels: number of points used in the interpolation scheme: $n_{\text{int}} = 2$ (red circles); and $n_{\text{int}} = 1$ (blue squares). In each case, 10^4 lines of sight have been distributed and binned uniformly with $\log(r/r_{\text{vir}})$, and 1σ error bars are shown. The analytic solution (black dots) at each impact parameter sampled is included in the left-hand panels. In the right-hand panels, the dotted horizontal line marks the 3 per cent error threshold.

of equal width, extending from the centre to the virial radius. Each particle is randomly placed in one of the radial bins with a probability proportional to the mass within that bin; the bin mass is found by appropriately integrating the density profile, given in equation (31). The lenses modelled for this purpose have a virial mass, and total mass, of $M_{\text{vir}}/M_{\odot} = 10^{14}$ and concentration parameter $c_{\Delta} = 7.2$. At a (lens) redshift of $z_L = 0.35$ and a virial overdensity of $\Delta_c = 200$, their virial radii are $0.55 h^{-1}$ Mpc. The results presented here are for a source redshift of $z_s = 0.8$. Figs 2–4 show the magnifications determined by ray tracing over a range of impact parameters changing one numerical parameter relative to a fiducial choice. The ray bundles are allowed to encounter the lens at a distance of up to twice the virial radius, which corresponds to an angular separation of 343 arcsec. The analytic solutions for image magnification and shear by a lens with the NFW profile are presented in Appendix D. Since the model lens is truncated at one virial radius, the metric on the exterior is given by the Schwarzschild metric, by Birkhoff's theorem. Thus, the analytic solution shown for $\mu(r)$ switches to that appropriate for a Schwarzschild lens outside this impact parameter.

Between the MRR and the truncation radius, the error remains fairly constant at 1 per cent. Outside the truncation radius, the error drops sharply by an order of magnitude, which implies that

the removal of mass outside this radius is primarily responsible for the aforementioned 1 per cent error. The size of the ray bundle, or, equivalently, the radius of the image or beam, has negligible effect on the ray-tracing results (see the top panels of Fig. 2). By varying the grid size (see the top panels of Fig. 3), we note that the MRR has a very strong dependence on the Fourier-grid resolution. Our interpretation is that the interpolation scheme used to measure the local gravitational field would smooth over the central cusp, causing the large errors here. We conclude that if small-scale structure is responsible for a caustic (high magnification), then this will be washed out. The MRR has a strong dependence on the number of points used to interpolate the values of the gravitational potential and its derivatives from the Fourier grid on which they are calculated, as shown in the bottom panels of Fig. 2. The use of more robust ray tracing, with a more accurate mean magnification value. However, the computation time rises approximately linearly with the number of interpolation points used, and the interpolation scheme suffers in the vicinity of density peaks. The latter issue should not pose too much of a problem when the lensing mass distribution is a large-scale structure, but computational efficiency presents a significant hurdle for ray-tracing procedures such as this. The parameters that most govern the accuracy of the

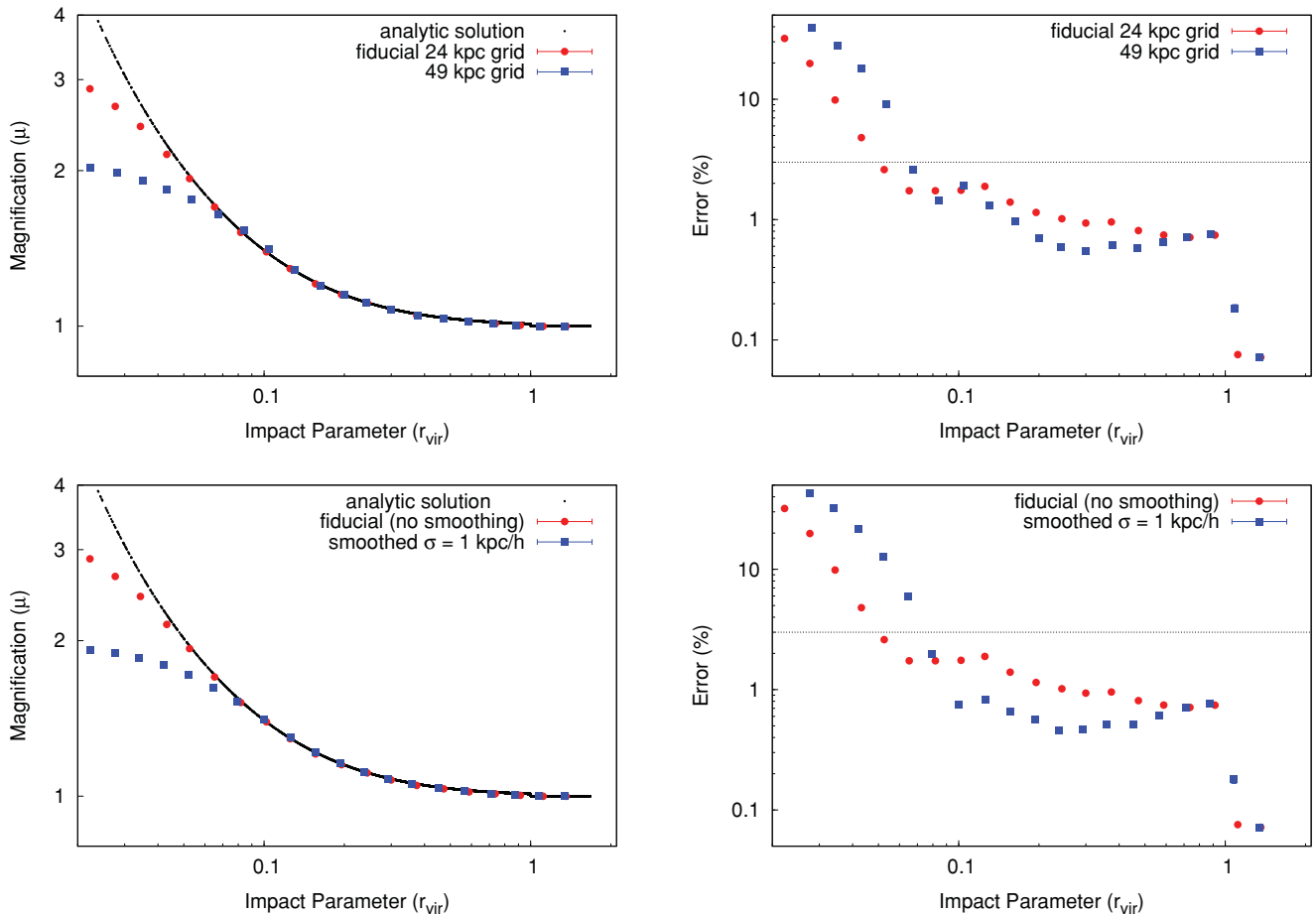


Figure 3. The radial dependence of magnification (μ ; left-hand panels) and the percentage error in the numerical magnification ($\Delta\mu/\mu$; right-hand panels) when ray tracing through a discretized NFW lens. Different values of numerical parameters are compared. Top panels: Fourier-grid resolution: $24 h^{-1}$ kpc (red circles); and $49 h^{-1}$ kpc (blue squares). Bottom panels: no smoothing (red circles) and smoothing with a filter of width $\sigma = 1 h^{-1}$ kpc (blue squares). In each case, 10^4 lines of sight have been distributed and binned uniformly with $\log(r/r_{\text{vir}})$, and 1σ error bars are shown. The analytic solution (black dots) at each impact parameter sampled is included in the left-hand panels. In the right-hand panels, the dotted horizontal line marks the 3 per cent error threshold.

ray-tracing scheme are the Fourier-grid size and mass smoothing length, which have essentially equivalent effects; assigning mass to a Fourier grid acts to spread it out over a fixed number of grid points. A CIC mass-assigning scheme is different from a Gaussian filter smoothing, but in essence, the larger the area over which mass is spread, the more density peaks are suppressed and the larger the error in the tests shown in Fig. 3. In the top panels of Fig. 4, we show that halving the Runge–Kutta step-size has a negligible effect, so half the Fourier-grid resolution is deemed sufficient. The model lens used for this test is subject to a few user-defined variables; a few convergence tests were run to ensure that these were not the cause of the observed features. Trialling different mass resolutions from 10^9 to $10^{11} M_\odot$ for a fixed halo virial mass, $M = 10^{14} M_\odot$, the results are shown in the middle panels of Fig. 4. We find that the resulting scatter increases from less than 1 per cent up to 10 per cent at a fixed impact parameter. One could equivalently say that the MRR is larger for haloes that are not as well resolved. The cosmological mass distributions in Section 5.1 have mass resolutions better than $10^{10} M_\odot$, so one can expect a low error in magnification even within dense regions. The number of bins that the lens is divided into is a choice that has negligible effect on the ray-tracing results, as shown in the bottom panels of Fig. 4. One is therefore reassured that the results of the ray tracing on the discretized NFW

profile are relevant to the results of ray tracing through cosmological mass distributions based on the fiducial parameter choices. Kling & Frittelli (2008) numerically integrate the null geodesic equations [with the adaptive step-size Runge–Kutta–Fehlberg method of order 4(5)] in order to test the accuracy of the thin-lens approximation, but only with reference to strong lensing by singular isothermal sphere and NFW (Navarro et al. 1995) mass profiles, both of which are relatively thin.

5 LARGE-SCALE STRUCTURE

5.1 Cosmological simulations

In order to construct the predicted probability distributions for the weak-lensing statistics numerically, numerous null geodesic equations are integrated through a cosmological mass distribution that is generated with N -body simulations. The cosmological simulations are carried out with the parallel Tree-PM SPH code GADGET2 (Springel 2005) using collisionless particles only. We adopt a Λ CDM cosmology, with the following values for the cosmological parameters: $\Omega_{\text{M},0} = 0.27$, $\Omega_{\Lambda,0} = 0.73$, $h = 0.71$, $\sigma_8 = 0.9$. The dark matter distribution is discretized into 256^3 particles distributed within a periodic box with a comoving length of $L_{\text{box}} =$

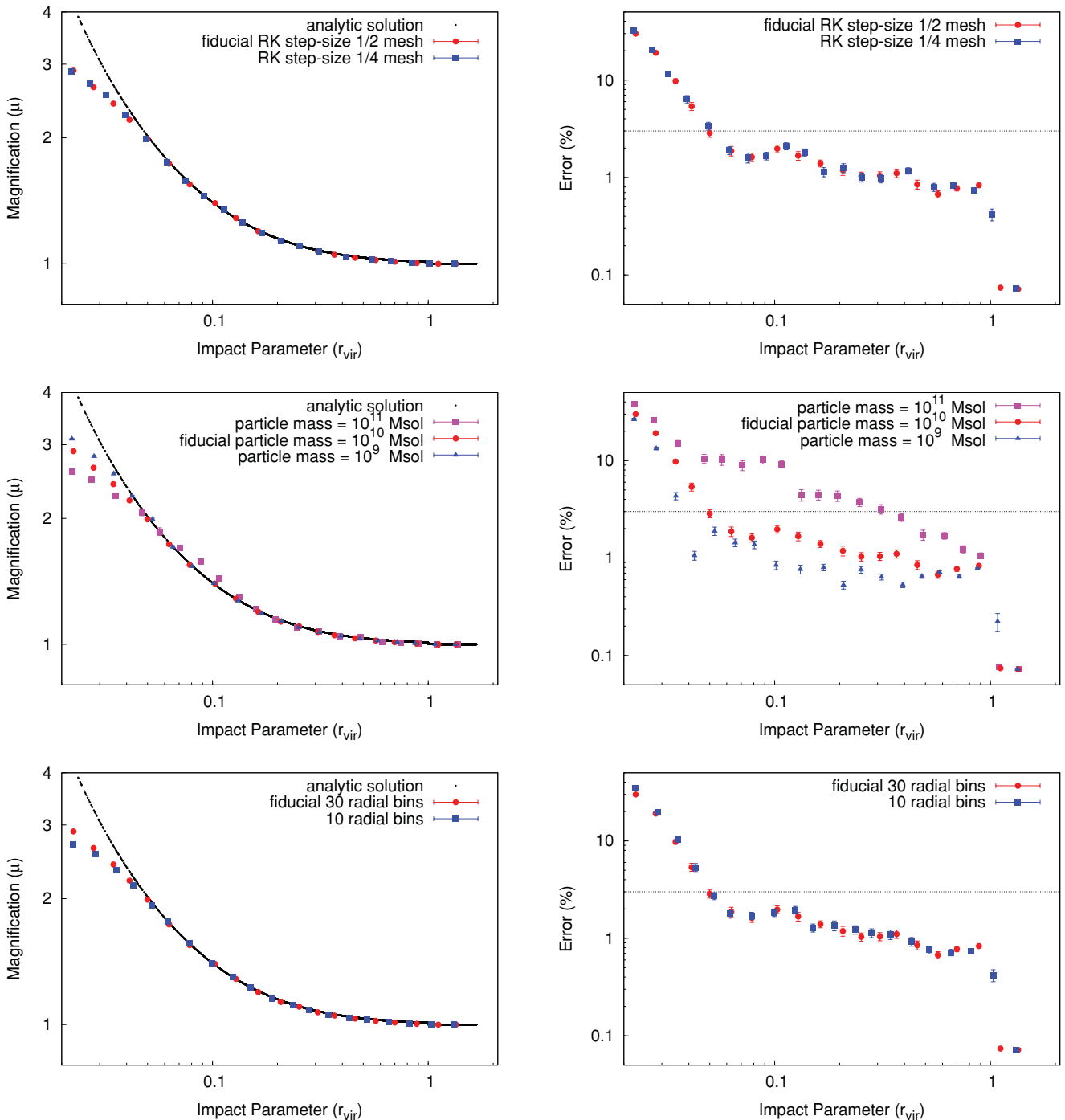


Figure 4. The radial dependence of magnification (μ ; left-hand panels) and the percentage error in the numerical magnification ($\Delta\mu/\mu$; right-hand panels) when ray tracing through a discretized NFW lens. Different values of numerical parameters are compared. Top panel: Runge–Kutta step-size that is half the Fourier-grid resolution (red circles) and for one-fourth the grid resolution (blue squares). Middle panels: mass resolution: $m_p/M_\odot = 10^{10}$ (red circles); $m_p/M_\odot = 10^{11}$ (pink squares); and $m_p/M_\odot = 10^9$ (blue triangles). Bottom panels: number of radial bins used for the lens discretization: 30 (red circles) and 10 (blue squares). In each case, 10^3 lines of sight have been distributed and binned uniformly with $\log(r/r_{\text{vir}})$, and 1σ error bars are shown. The analytic solution (black dots) at each impact parameter sampled is included in the left-hand panels. In the right-hand panels, the dotted horizontal line marks the 3 per cent error threshold.

$50 h^{-1}$ Mpc, resulting in a mass resolution of $m_p = 6.3 \times 10^8 M_\odot$; the initial displacements are in a ‘glass’ configuration. The simulations begin at an initial redshift of $z_i = 39$, with a redshift-dependent gravitational force softening length of $\epsilon_{\text{co}} = 16 h^{-1}$ kpc (Plummer equivalent).

The space between an observer and source is divided up into individual regions, each modelled by a snapshot of a cosmological simulation at an appropriate redshift. The snapshot cadence, Δz , is chosen such that the light traveltime corresponds to the length of the boxes. The line-of-sight integrated comoving distance between

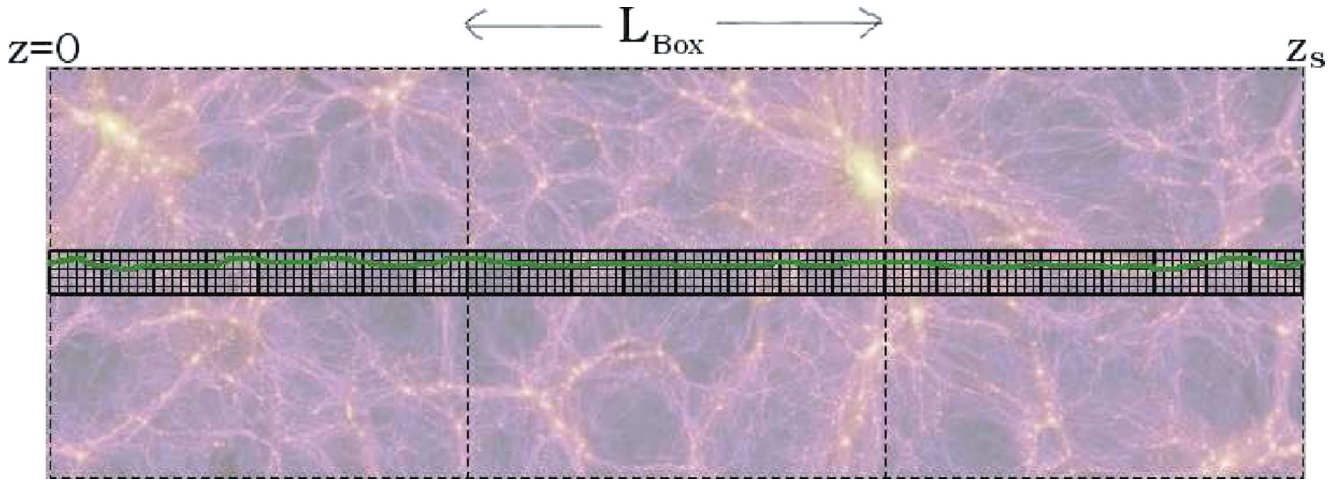


Figure 5. A two-dimensional schematic diagram of the ray-tracing method. Large simulation snapshots (dashed lines; three shown here) of length L_{box} fill up the space from the observer, $z = 0$, to the source plane at z_s . The small cubes (thick lines) from within these boxes form a prism of lensing mass. The mass in each cube is distributed on to Fourier grids (thin lines) before calculating the gravitational potential and derivatives in order to numerically integrate the path (green) of a photon.

an observer and source at $z = z_s$ is

$$D_c = c \int_0^{z_s} \frac{dz}{H(z)}. \quad (33)$$

Since this cannot be easily evaluated in general, we instead assume that the differences between the redshifts of adjacent boxes are small, and thus

$$L_{\text{box}} = \frac{c \Delta z}{H(z)}, \quad (34)$$

which is easily rearranged to determine the snapshot cadence. A total of 28 boxes are required to fill the space between an observer and a source at $z \approx 0.5$.

Note that the scalefactor at the position of a photon is required to integrate the null geodesic equations. This scalefactor is *not* identified with the ‘average’ redshift of the current snapshot being traced through; instead, it is derived from the look-back time (see equation 3.5) and evolves during the integration through the box. That is to say, it is assumed that in the time it takes for a photon to traverse a box, the comoving scale of the structure remains constant; however, the physical scalelength changes. As a sanity check, the numerically derived value of the scalefactor at each box interface is compared to the redshift of the appropriate snapshot.

5.2 The sampling region

In order to avoid repeated structure, a number of precautions were taken. Nine independent simulations were run, resulting in nine separate realizations. The snapshot for each required redshift was chosen randomly from among the nine realizations. The chosen box was then randomly translated and rotated 90° about any/all of the axes. From each $50 h^{-1}$ Mpc box, we selected the lensing mass formed by particles within a prism $6.25 h^{-1}$ Mpc across the sky and $50 h^{-1}$ Mpc along the line of sight. This is split into eight cubes each of volume $V = 6.25^3 (h^{-1} \text{Mpc})^3 \approx 244 (h^{-1} \text{Mpc})^3$. Each of these has its mass placed on a 128^3 point grid, using the CIC algorithm. We apply an FFT to these boxes with zero-padding so that the density field (and the derivatives of the gravitational potential) due to structure *within the box only* is determined on a scale of $49 h^{-1}$ kpc. Note here that the simulation is run on a larger box such that the large-scale modes are included in the formation of

structure, but we only use a smaller portion of the box for the lensing (see Fig. 5 for a cartoon diagram). The null geodesic equations of the eight rays and one anchor of each ray bundle are numerically integrated using the methods described in Section 3.4.

Lines of sight that fall too close to the edge of the boxes will be artificially sheared, so assuming that most of the lensing occurs due to mass within $0.5 h^{-1}$ Mpc, we only send out ‘beams’ that will fall within the central $5.25 \times 5.25 (h^{-1} \text{Mpc})^2$ region at the source redshift. For a source redshift of $z_s = 0.5$, with an angular diameter distance of approximately $900 h^{-1}$ Mpc, this means that the area of sky sampled is about $0.33 \times 0.33 \text{ deg}^2$ or 0.0005 per cent of the entire sky. To increase the sampling area, this entire procedure is used to trace the paths of 10 000 bundles, then repeated for another 10 000 bundles using another lensing mass distribution sampled from the same set of simulations.

5.3 Numerically determining μ PDFs

Using ray-tracing procedures to construct a magnification probability distribution is effectively equivalent to calculating the angular diameter distance in different directions out to the same comoving distance. The distribution of angular diameter distances for a given source redshift has been investigated by Hadrović & Binney (1997). In the extremal case of a large beam-size, and therefore, large separations between rays, the angular diameter distances would be the same in all directions and the ‘distribution’ would be a single peak at $D_{\text{fb}}(z)$, the average FLRW value, implying homogeneity on those scales. However, if the beam-size is small enough, then the inhomogeneities induce a distribution. Each ray bundle probes a single line of sight. More specifically, it describes the lensing that has affected a single image of a fixed size on the sky. The number of bundles that exhibit a magnification of μ is thus proportional to the probability that an *image* is magnified by μ . However, the statistical quantity of interest is the magnification probability distribution for *sources*. Therefore, the number counts that are used to produce the magnification probability histograms presented in Section 5.4 are weighted by the area covered by the beam at the source plane, or, equivalently, the inverse of the magnification:

$$P(\mu) d\mu = \frac{F(\mu, \mu + d\mu)}{\mu}, \quad (35)$$

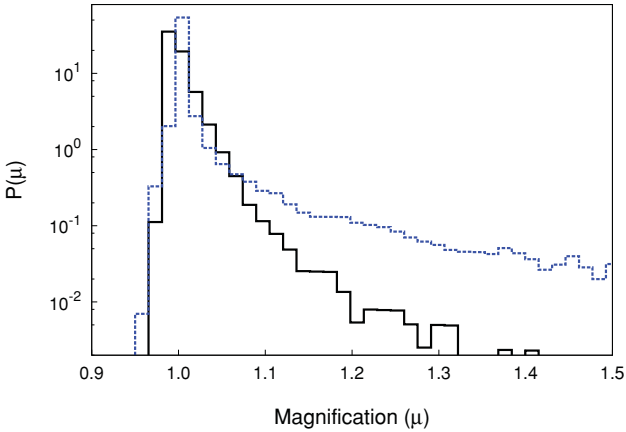


Figure 6. The magnification probability distribution for a source at redshift $z = 0.5$ as predicted by the multiple-lens-plane RBM (blue dashed line) and by the three-dimensional equivalent (black solid line).

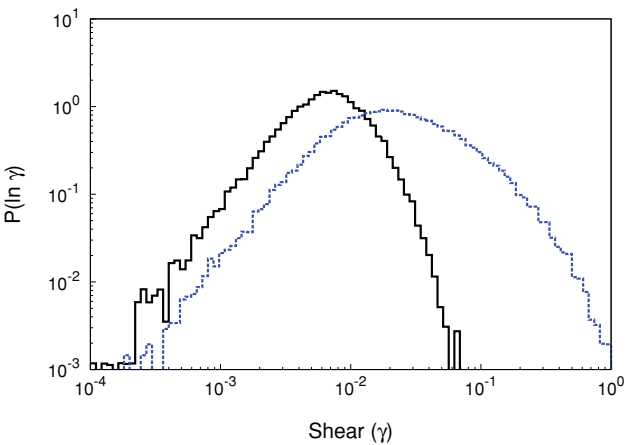


Figure 7. The shear probability distribution for a source at redshift $z = 0.5$ as predicted by the multiple-lens-plane RBM (blue dashed line) and by the three-dimensional equivalent (black solid line).

where $F(\mu_1, \mu_2)$ is the fraction of all ray bundles for which $\mu_1 < \mu < \mu_2$. Similarly, the mean and standard deviation of these properties are also weighted.

5.4 Comparison of the PDFs produced with and without lens planes

The predicted probability distributions of magnification and shear are constructed by ray-tracing 2×10^4 bundles through the three-dimensional mass distribution described above. The results, shown in Figs 6 and 7, are compared to the probability distributions constructed with the multiple-lens-plane RBM using 5×10^4 bundles. However, not all ray bundles are included in the analysis. The RBM is very well suited to the weak-lensing limit and provides a computationally efficient alternative to grid-based ray-shooting methods; however, it underestimates the magnification in cases where multiple imaging is expected as only one image contributes to the magnification of each source. For this reason, rays that fall within a minimum distance of a lens (remembering that a distribution of point masses describes the lensing mass) are excluded from the analysis. This affects the high magnification probabilities deduced, but does not significantly affect the weak-lensing analysis (Fluke,

Webster & Mortlock 2002). The RBM avoids the danger of artificial shear due to a source pixel collecting light rays that have passed near the edge of a shooting grid. If a ray bundle were to suffer from neither convergence nor shear, it would obtain the minimal magnification, $\mu_{\text{eb,min}} = 1$, or, equivalently, $\mu_{\text{fb,min}} = D_{\text{fb}}^2(z_s)/D_{\text{eb}}^2(z_s)$ (see Appendix E). For a source redshift of $z = 0.5$, this minimum magnification is ≈ 0.965 ; the relevant angular diameter distances have been determined with the aid of the `Angsiz` routine (Kayser, Helbig & Schramm 1997). Those bundles that produce magnifications below this minimum value represent the demagnified components of a multiple-image system, a possible consequence of strong lensing. These will highly underestimate the total magnification of the associated source, and so are also excluded in both methods. On the other hand, if a magnified image is traced back to the source plane, but belongs to a multiple-image system, it will not be identified as such. Although it will also underestimate the total magnification, it will generally do so by a negligible amount. The ray-tracing method developed in this work does not produce any bundles that must be excluded.

The average magnification predicted by both methods is close to unity, as required by flux conservation (see equation 14). More precisely, the multiple-lens-plane approach finds $\bar{\mu} = 1.0199$, while the three-dimensional approach finds a mean magnification of $\bar{\mu} = 0.9994$. Using the three-dimensional method to analyse lensing by large-scale structure, we find that large magnifications are not produced, as shown in Fig. 6. The slope of the differential magnification probability distribution is found to be much steeper than for the RBM for the regime $1.1 < \mu < 1.5$. The difference between the two methods can also be quantified by standard deviation, found to be $\sigma_\mu = 0.205$ from the multiple-lens-plane approach and $\sigma_\mu = 0.021$ from the three-dimensional approach, an order of magnitude lower. To understand the reason of this difference, we also plot the probability distribution for shear, shown in Fig. 7. While the overall shape of the distribution function is similar as derived by the two methods, the multiple-lens-plane method measures more high shear values and less low shear values.

The projection of matter on to multiple-lens planes may have artificially increased the shearing effect of cosmological lenses. However, the effect of shot-noise in the standard RBM is identified as another possible reason for the discrepancy. When the three-dimensional approach is used, the gravitational potential is calculated by means of Fourier methods. In contrast, the multiple-lens-plane approach determines the potential field at the location of each ray, but adding the potential due to each simulation particle in the plane individually. Each particle in the simulation represents some underlying smooth mass distribution, but by treating them as point masses, the method is susceptible to the effects of shot-noise. Recently, Takahashi et al. (2011) discussed the effects of shot-noise on the variance of the convergence found by ray tracing through N -body simulations. Although they did not use the same ray-bundle approach as we do here, they apply a multiple-lens-plane method with an FFT for calculating the gravitational potential in each plane; they compare their results for a range of Fourier-grid resolutions (see fig. 2 of their paper). When the grid resolution is large enough to smear out structure, the variance of the convergence falls below theoretical predictions; although our choice of statistic is different, our results agree with this interpretation (see Fig. 3 in Section 4.2). Interestingly, a very small grid resolution ($< 5 h^{-1}$ kpc) leads to a variance that is larger than the theoretical prediction, a result which they attribute to shot-noise. We agree with this interpretation, noting that Fourier methods applied to grid resolutions that are much smaller than the mean interparticle distance would resemble a direct

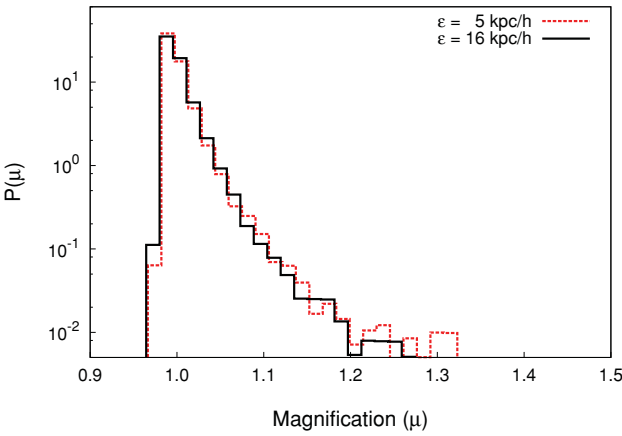


Figure 8. The magnification probability distribution for a source at redshift $z = 0.5$ as predicted by the three-dimensional method. Two different force-softening lengths applied in the N -body simulations are compared: $\epsilon = 5 h^{-1}$ kpc (red dashed line); and $\epsilon = 16 h^{-1}$ kpc (black solid line).

summation as employed by the multiple-lens-plane approach in this work.

The μ PDF predicted by the three-dimensional method is subject to certain choices of numerical parameters, some of which have been discussed above. Thus, we test the parameters that are most likely to have an impact on the cosmological lensing results presented above. For example, a parameter that was not relevant to the tests presented in Section 4 is the force-softening length chosen for the cosmological N -body simulation. We re-run the simulation described earlier but with a force-softening length reduced to $\epsilon = 5 h^{-1}$ kpc. We sample 3×10^4 lines of sight through the mass distribution determined with this simulation, and in Fig. 8, we compare the μ PDF to the result for the three-dimensional method shown in Fig. 6. For each, the Fourier-grid resolution is $49 h^{-1}$ kpc. The similarities in the PDFs reassures us that any smoothing of structure below $16 h^{-1}$ kpc is not responsible for any error in the PDFs measured by the three-dimensional method.

In addition, as the Fourier-grid scale is reduced, the numerical solution is expected to be more accurate, with the caveat that it remains large enough to prevent the effects of shot-noise. In Fig. 9, we compare two different Fourier-grid resolutions: $24 h^{-1}$ kpc for

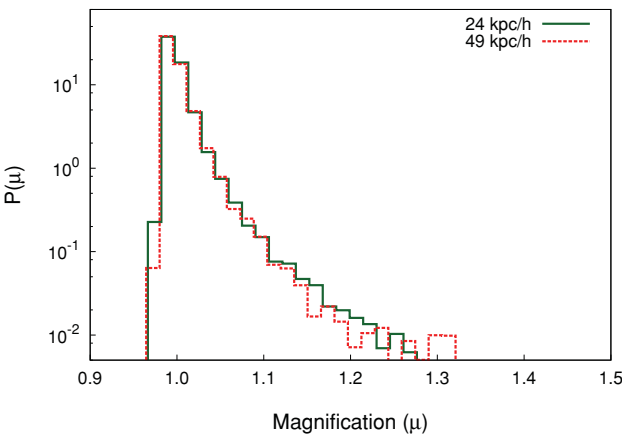


Figure 9. The magnification probability distribution for a source at redshift $z = 0.5$ as predicted by the three-dimensional method. Two different Fourier-grid resolutions are compared: $24 h^{-1}$ kpc (green solid line); and $49 h^{-1}$ kpc (red dashed line).

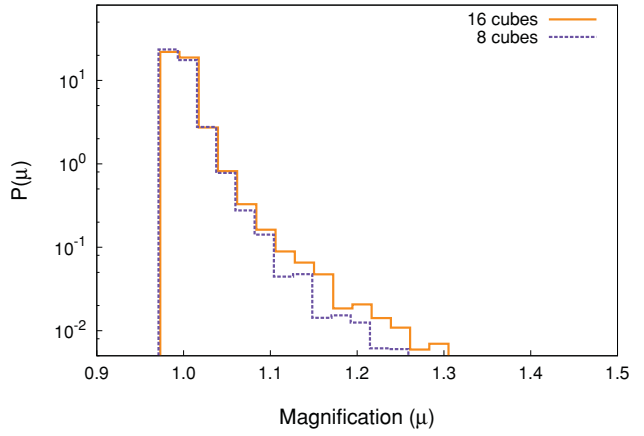


Figure 10. The magnification probability distribution for a source at redshift $z = 0.5$ as predicted by the three-dimensional method. The same Fourier-grid resolution ($24 h^{-1}$ kpc) is created, but excising either eight cubes (purple dashed line) or 16 cubes (yellow solid line) from each simulation box.

which 9×10^4 lines of sight have been sampled, and $49 h^{-1}$ kpc for which 3×10^4 lines of sight have been sampled. Both tests are run on simulations with a force-softening length reduced to $\epsilon = 5 h^{-1}$ kpc, which are only able to reliably describe structure on scales larger than $20 h^{-1}$ kpc. The differences are negligible, which demonstrate that most of the weak lensing results from structure above $49 h^{-1}$ kpc scales. Structures on scales larger than $24 h^{-1}$ kpc that are able to produce strong or even ‘moderate’ lensing are rare.

We recognize that there are multiple ways to create the same Fourier-grid resolution. If the number of cubes taken from the simulation boxes is doubled, but the number of Fourier-grid points halved, the resolution does not change. However, only a quarter of the patch of sky would be sampled, and the computational runtime would double. On the upside, the memory usage reduces to an eighth, which is a significant advantage for such a computationally demanding approach. In Fig. 10, we show the result of doubling the number of cubes in such a manner; the Fourier-grid resolution is $24 h^{-1}$ kpc. A total of 3×10^4 lines of sight have been sampled for the method using eight cubes, while 6×10^4 lines of sight have been sampled for the method using 16 cubes. Note that this was not tested on the compact lens models in Section 4 since cubes are not excised from simulations as they are when analysing cosmological lensing. We are satisfied that the choice of eight cubes for our previous results (see Figs 6 and 7) has no bearing on the results.

6 SUMMARY AND DISCUSSION

Modelling the magnification probability distribution of background sources due to gravitational lensing relies on the application of ray-tracing methods. This work has taken the first steps towards making a direct comparison between the predictions of the multiple-lens-plane RBM and one that does not invoke the thin-lens approximation; instead, the null geodesic equations are integrated. The efficiency and accuracy of this computationally challenging approach can be improved by careful choices of numerical parameters; therefore, the results are analysed for the behaviour of the ray-tracing code in the vicinity of Schwarzschild and NFW lenses. A range of tests were able to pin down the numerical parameters that play a critical role in the predicted statistics. The behaviour of the ray bundles in the vicinity of a Schwarzschild lens demonstrated that the method can reproduce large magnifications, given sufficient

spatial resolution. The limitations are dominated by the spatial resolution of the Fourier grid and the mass resolution of the discretized lens.

Comparisons to a multiple-lens-plane algorithm are drawn in the context of cosmological mass distribution for a source redshift of $z_s = 0.5$. The weak-lensing statistics predicted by ray tracing through simulated cosmological mass distributions found significant differences compared to the results from the original RBM approach. Either the use of multiple-lens planes or the use of shot-noise is responsible for the observed differences. To clarify the dominant factor, a multiple-lens-plane RBM that applies a two-dimensional Fourier method at each lens plane is proposed as the next step towards the direct comparison.

The method developed here presents a computational challenge as the three-dimensional FFTs prove memory-expensive, but is justified by the need to quantify the multiple-lens-plane approximation. We are, as yet, unable to sample the large number of lines of sight required to model the intermediate-magnification ($2 < \mu < 20$) region where Rauch et al. (1992) had identified the feature present only in two-dimensional lens models.

We now discuss future applications of the ray-tracing method that are outside the scope of this work. For example, proposed large surveys have the measurement of cosmic shear, with particular focus on the determination of the nature of dark energy, as one of their main science drivers, using a combination of a large area of sky coverage and high-precision photometric redshifts. These include the ground-based Panoramic Survey Telescope and Rapid Response System,² the VST-Kilo-Degree Survey,³ the Dark Energy Survey,⁴ the Large Synoptic Survey Telescope⁵ as well as the space-based *Euclid* (Laureijs 2009)⁶ and the Joint Dark Energy Mission,⁷ which has recently been rebranded as the Wide-Field InfraRed Survey Telescope. The method developed in this work has the potential to quantify the effects of multiple-lens-plane techniques on the theoretical predictions for cosmic-shear measurements. Another alternative to ray tracing is to retain the three-dimensional mass distribution, but assume that the deflections are small enough to satisfy the Born approximation. Here, the matter that is integrated along the (un-deflected) line of sight is solely responsible for the convergence. Over larger and larger distances, the Born approximation becomes less and less accurate; several studies have found the requirement for corrections in the construction of the shear power spectrum and higher order bispectrum (e.g. Van Waerbeke et al. 2001; Shapiro & Cooray 2006). We envisage that the three-dimensional method could be used to make a one-to-one comparison with the Born approximation, just as we have done here with the multiple-lens-plane method.

Finally, with a larger number of ray bundles and greater sky sampling, we could turn our attention to higher order statistics. Flexion is the third-order effect in gravitational lensing and is effectively the gradient of the shear component (see Goldberg & Bacon 2005). It has recently been demonstrated that flexion can be modelled using a RBM (Fluke & Lasky 2011); this presents an exciting future application of the method, but surely it is even more necessary to justify the use of the multiple-lens-plane formalism.

² <http://pan-starrs.ifa.hawaii.edu>

³ <http://www.astro-wise.org/projects/KIDS/>

⁴ <http://www.darkenergysurvey.org/>

⁵ <http://www.lsst.org>

⁶ <http://sci.esa.int/euclid>

⁷ <http://jdem.lbl.gov/> and <http://jdem.gsfc.nasa.gov/>

ACKNOWLEDGMENTS

MK acknowledges support from the University of Sydney Faculty of Science Postgraduate Award, as well as a fellowship from the European Commission's Framework Programme 7, through the Marie Curie Initial Training Network CosmoComp (PITN-GA-2009-238356), and would like to thank the Centre for Astrophysics and Supercomputing at the Swinburne University of Technology for their hospitality and for the use of the Green Machine. PDL is supported by the Alexander von Humboldt Foundation. This work is undertaken as part of the CCI (www.thecci.org), and funded by the Australian Research Council Discovery Project DP0665574.

REFERENCES

- Astier P. et al., 2006, A&A, 447, 31
 Babul A., Lee M. H., 1991, MNRAS, 250, 407
 Bartelmann M., Loeb A., 1996, ApJ, 457, 529
 Blandford R., Narayan R., 1986, ApJ, 310, 568
 Canizares C. R., 1981, Nat, 291, 620
 Coe D., 2010, preprint (arXiv:1005.0411)
 Cole S. et al., 2005, MNRAS, 362, 505
 Couchman H. M. P., Barber A. J., Thomas P. A., 1999, MNRAS, 308, 180
 Das S., Ostriker J. P., 2006, ApJ, 645, 1
 Davis M., Huchra J., Latham D. W., Tonry J., 1982, ApJ, 253, 423
 Dyer C. C., 1977, MNRAS, 180, 231
 Dyer C. C., Roeder R. C., 1972, ApJ, 174, L115
 Dyer C. C., Roeder R. C., 1974, ApJ, 189, 167
 Fluke C. J., 1999, PhD thesis, The University of Melbourne
 Fluke C. J., Lasky P. D., 2011, MNRAS, 416, 1616
 Fluke C. J., Webster R. L., Mortlock D. J., 1999, MNRAS, 306, 567
 Fluke C. J., Webster R. L., Mortlock D. J., 2002, MNRAS, 331, 180
 Futamase T., Sasaki M., 1989, Phys. Rev. D, 40, 2502
 Goldberg D. M., Bacon D. J., 2005, ApJ, 619, 741
 Gunnarsson C., Dahlgren T., Goobar A., Jönsson J., Mörtzell E., 2006, ApJ, 640, 417
 Hadrović F., Binney J., 1997, preprint (arXiv:astro-ph/9708110)
 Hamana T., Martel H., Futamase T., 2000, ApJ, 529, 56
 Hilbert S., Gair J. R., King L. J., 2011, MNRAS, 412, 1023
 Hirata C. M., Holz D. E., Cutler C., 2010, Phys. Rev. D, 81, 124046
 Hobson M. P., Efstatouli G. P., Lasenby A. N., 2006, General Relativity. Cambridge Univ. Press, Cambridge
 Hockney R. W., Eastwood J. W., 1988, Computer Simulation Using Particles. Hilger, Bristol
 Holz D. E., Hughes S. A., 2005, ApJ, 629, 15
 Holz D. E., Linder E. V., 2005, ApJ, 631, 678
 Holz D. E., Wald R. M., 1998, Phys. Rev. D, 58, 063501
 Jain B., Lima M., 2011, MNRAS, 411, 2113
 Jain B., Seljak U., White S., 2000, ApJ, 530, 547
 Jaroszynski M., Park C., Paczynski B., Gott J. R., III, 1990, ApJ, 365, 22
 Jönsson J., Goobar A., Mörtzell E., 2007, ApJ, 658, 52
 Jönsson J., Kronborg T., Mörtzell E., Sollerman J., 2008, A&A, 487, 467
 Jönsson J., Mörtzell E., Sollerman J., 2009, A&A, 493, 331
 Kantowski R., 1969, ApJ, 155, 89
 Kasai M., Futamase T., Takahara F., 1990, Phys. Lett. A, 147, 97
 Kayser R., Refsdal S., Stabell R., 1986, A&A, 166, 36
 Kayser R., Helbig P., Schramm T., 1997, A&A, 318, 680
 Kling T. P., Frittelli S., 2008, ApJ, 675, 115
 Kovner I., 1987, ApJ, 316, 52
 Laureijs R., 2009, preprint (arXiv:0912.0914)
 Le Brun V., Smette A., Surdej J., Claeskens J.-F., 2000, A&A, 363, 837
 Lee M. H., Paczynski B., 1990, ApJ, 357, 32
 Lee M. H., Babul A., Kofman L., Kaiser N., 1997, ApJ, 489, 522
 Linder E. V., 1988, A&A, 206, 190
 Marković D., 1993, Phys. Rev. D, 48, 4738
 Navarro J. F., Frenk C. S., White S. D. M., 1995, MNRAS, 275, 720
 Paczynski B., Wambsganss J., 1989, ApJ, 337, 581

- Peacock J. A., 1982, MNRAS, 199, 987
 Pei Y. C., 1993, ApJ, 403, 7
 Premadi P., Martel H., Matzner R., Futamase T., 2001, ApJS, 135, 7
 Rauch K. P., Mao S., Wambsganss J., Paczynski B., 1992, ApJ, 386, 30
 Sachs R., 1961, Proc. R. Soc. A, 264, 309
 Schechter P., 1976, ApJ, 203, 297
 Schneider P., Weiss A., 1988, ApJ, 330, 1
 Seitz S., Schneider P., Ehlers J., 1994, Class. Quantum Gravity, 11, 2345
 Shang C., Haiman Z., 2011, MNRAS, 411, 9
 Shapiro C., Cooray A., 2006, J. Cosmol. Astropart. Phys., 3, 7
 Shapiro C., Bacon D. J., Hendry M., Hoyle B., 2010, MNRAS, 404, 858
 Springel V., 2005, MNRAS, 364, 1105
 Takahashi R., Oguri M., Sato M., Hamana T., 2011, ApJ, 742, 15
 Tomita K., 1998, Prog. Theor. Phys., 100, 79
 Turner E. L., Ostriker J. P., Gott J. R., III, 1984, ApJ, 284, 1
 Vale C., White M., 2003, ApJ, 592, 699
 Van Waerbeke L., Hamana T., Scoccimarro R., Colombi S., Bernardeau F., 2001, MNRAS, 322, 918
 Vietri M., Ostriker J. P., 1983, ApJ, 267, 488
 Wambsganss J., 1990, PhD thesis, Thesis Ludwig-Maximilians-Univ., Munich (Germany)
 Wambsganss J., Cen R., Xu G., Ostriker J. P., 1997, ApJ, 475, L81
 Wambsganss J., Cen R., Ostriker J. P., 1998, ApJ, 494, 29
 Wambsganss J., Bode P., Ostriker J. P., 2005, ApJ, 635, L1
 Watanabe K., Tomita K., 1990, ApJ, 355, 1
 Weinberg S., 1976, ApJ, 208, L1
 White M., Hu W., 2000, ApJ, 537, 1
 Wright C. O., Brainerd T. G., 2000, ApJ, 534, 34
 Wyithe J. S. B., Yan H., Windhorst R. A., Mao S., 2011, Nat, 469, 181
 Yoo C., Ishihara H., Nakao K., Tagoshi H., 2008, Prog. Theor. Phys., 120, 961

APPENDIX A: CHRISTOFFEL SYMBOLS

The expanding weak-field metric presented in equation (18) has the following non-zero Christoffel symbols:

$$\begin{aligned}
 \Gamma_{tt}^x &= \frac{1}{a^3} \phi_{,x}, \\
 \Gamma_{tt}^y &= \frac{1}{a^3} \phi_{,y}, \\
 \Gamma_{tt}^z &= \frac{1}{a^3} \phi_{,z}, \\
 \Gamma_{tx}^t &= -\frac{\dot{a}}{a^2} \phi, \\
 \Gamma_{tx}^x &= \Gamma_{ty}^y = \Gamma_{tz}^z = \frac{\dot{a}}{a^2} (a + \phi), \\
 \Gamma_{tx}^t &= \Gamma_{yy}^x = \Gamma_{zz}^x = \frac{1}{a} \phi_{,x}, \\
 \Gamma_{xx}^x &= \Gamma_{xy}^y = \Gamma_{xz}^z = -\frac{1}{a} \phi_{,x}, \\
 \Gamma_{ty}^t &= \Gamma_{xx}^y = \Gamma_{zz}^y = \frac{1}{a} \phi_{,y}, \\
 \Gamma_{yy}^y &= \Gamma_{yx}^x = \Gamma_{yz}^z = -\frac{1}{a} \phi_{,y}, \\
 \Gamma_{tz}^t &= \Gamma_{xx}^z = \Gamma_{yy}^z = \frac{1}{a} \phi_{,z}, \\
 \Gamma_{zz}^z &= \Gamma_{zx}^x = \Gamma_{zy}^y = -\frac{1}{a} \phi_{,z}, \\
 \Gamma_{xx}^t &= \Gamma_{yy}^t = \Gamma_{zz}^t = \dot{a}(a + \phi).
 \end{aligned} \tag{A1}$$

Note that x denotes x^1 , y denotes x^2 and z denotes x^3 . The Christoffel symbols for this metric are dependent not only on the gradients of the gravitational potential ϕ , but also on ϕ itself. However, the weak-

field condition requires that the magnitude of the perturbations satisfies $\phi \ll a$. The geodesic equations – the second-order differential equations for the four coordinates – are then constructed.

APPENDIX B: THE INTERPOLATION SCHEME

Here we only describe the scheme for the evaluation of $\phi(x_\star^1, x_\star^2, x_\star^3)$, given the gridded values $\phi(x^1, x^2, x^3)$, but the same method is applied to evaluate the derivatives of the potential. The scheme is not strictly tricubic interpolation, but a three-dimensional version of the bicubic spline. Instead, it initially performs a one-dimensional spline to compute the derivative with respect to the line of sight; that is, it fits a spline to find $d\phi(x^1, x^2, x^3)/dx^3$ across the entire grid. This is only done once for each lensing mass distribution. Each time the local values need to be found, the scheme identifies the gridded values that include n_{int} points on either side of the current location for each dimension, that is, a $(2n_{\text{int}})^3$ mesh grid. Then, the scheme performs the following steps:

- (i) The gridded derivative is interpolated across the chosen dimension, in this case the x^3 -dimension, to find $\phi(x^1, x^2, x_\star^3)$, that is, the value with the current x^3 -coordinate of the photon specified, but the other coordinates corresponding to grid points. $(2n_{\text{int}})^2$ interpolations are required.
- (ii) Another set of $2n_{\text{int}}$ one-dimensional splines are performed, this time across the x^1 -axis, to find $d\phi(x^1, x^2, x_\star^3)/dx^1$.
- (iii) $2n_{\text{int}}$ interpolations along the x^1 -axis to determine $\phi(x_\star^1, x^2, x_\star^3)$.
- (iv) A single one-dimensional spline across the x^2 -axis is used to find $d\phi(x_\star^1, x^2, x_\star^3)/dx^2$.
- (v) Finally, a single interpolation along the x^2 -axis allows one to evaluate $\phi(x_\star^1, x_\star^2, x_\star^3)$.

APPENDIX C: SCHWARZSCHILD LENS

A single point of infinite density is one of the simplest lens models, and is often used to model a spherically symmetric lens for idealized analytical studies. The relevant (angular) scalelength for a so-called Schwarzschild lens of mass M is the Einstein radius

$$\theta_{\text{Ein}} = \sqrt{\frac{D_{\text{ds}}}{D_{\text{d}} D_{\text{s}}}} \frac{\sqrt{4GM}}{c}. \tag{C1}$$

At the lens plane, this corresponds to a physical scalelength given by

$$r_{\text{Ein}} = \theta_{\text{Ein}} D_{\text{d}}. \tag{C2}$$

The gravitational lensing quantities of interest are found by combining the derivatives of this potential, as described in Section 2. They are defined in terms of a dimensionless radial distance, $x = r/r_{\text{Ein}}$. All lines of sight probe regions outside the lens, so the convergence is zero. The solution for the shear for images lensed by a Schwarzschild lens, γ_{Schw} , is

$$\gamma_{\text{Schw}}(x) = x. \tag{C3}$$

The analytic solution for the magnification for an image at any location, μ_{Schw} , is

$$\mu_{\text{Schw}}(x) = \left(1 - \frac{1}{x^4}\right)^{-1}. \tag{C4}$$

APPENDIX D: NFW LENS

The NFW profile, given in equation (31), can be considered a thin lens for cases where the observer, lens and source are separated by large angular diameter distances. The following analytic solutions, equations (D1)–(D8), are therefore derived from projected surface densities. A dimensionless radial distance, $x = r/r_s$, has been adopted. Here, the quantities ρ_c , r_s , δ_c and Σ_{crit} are those defined in equations (22), (31), (32) and (4), respectively. Following Wright & Brainerd (2000) and Coe (2010), the analytic solution for the radial dependence of the convergence is given by

$$\kappa_{\text{NFW}}(x) = \frac{r_s \delta_c \rho_c}{\Sigma_{\text{crit}}} K(x), \quad (\text{D1})$$

where $K(x)$ is given by

$$K(x) = \begin{cases} \frac{2}{(x^2 - 1)} \left(1 - \frac{2}{\sqrt{1-x^2}} \tanh^{-1} \sqrt{\frac{1-x}{1+x}} \right) & \text{if } x < 1 \\ \frac{2}{3} & \text{if } x = 1 \\ \frac{2}{(x^2 - 1)} \left(1 - \frac{2}{\sqrt{x^2 - 1}} \tan^{-1} \sqrt{\frac{x-1}{1+x}} \right) & \text{if } x > 1 \end{cases}. \quad (\text{D2})$$

By integrating equation (D1) over the area within r , one finds the mass within a cylinder of radius r

$$M_{\text{NFW,cyl}}(x) = 4\pi r_s^3 \delta_c \rho_c C(x), \quad (\text{D3})$$

where $C(x)$ is given by

$$C(x) = \ln \frac{x}{2} + \begin{cases} \frac{1}{\sqrt{1-x^2}} \cosh^{-1} \frac{1}{x} & \text{if } x < 1 \\ 1 & \text{if } x = 1 \\ \frac{1}{\sqrt{x^2 - 1}} \cos^{-1} \frac{1}{x} & \text{if } x > 1 \end{cases}. \quad (\text{D4})$$

The radial dependence of shear is thus given by

$$\gamma_{\text{NFW}}(x) = \frac{r_s \delta_c \rho_c}{\Sigma_{\text{crit}}} G(x), \quad (\text{D5})$$

where $G(x)$ is given by

$$G(x) = \begin{cases} g_<(x) & \text{if } x < 1 \\ \left[\frac{10}{3} + 4 \ln \left(\frac{1}{2} \right) \right] & \text{if } x = 1 \\ g_>(x) & \text{if } x > 1 \end{cases}. \quad (\text{D6})$$

The functions $g_<(x)$ and $g_>(x)$ are given by

$$g_<(x) = \frac{8 \tanh^{-1} \sqrt{(1-x)/(1+x)}}{x^2 \sqrt{1-x^2}} + \frac{4}{x^2} \ln \left(\frac{x}{2} \right) - \frac{2}{(x^2 - 1)} + \frac{4 \tanh^{-1} \sqrt{(1-x)/(1+x)}}{(x^2 - 1) \sqrt{1-x^2}} \quad (\text{D7})$$

and

$$g_>(x) = \frac{8 \tan^{-1} \sqrt{(x-1)/(1+x)}}{x^2 \sqrt{x^2 - 1}} + \frac{4}{x^2} \ln \left(\frac{x}{2} \right) - \frac{2}{(x^2 - 1)} + \frac{4 \tan^{-1} \sqrt{(x-1)/(1+x)}}{(x^2 - 1)^{3/2}}. \quad (\text{D8})$$

Combining these with equations (D1) and (D5) with equations (3) and (8) allows one to determine the analytic value of the magnification, μ , of an image at a given projected distance from the centre of the NFW lens.

APPENDIX E: FULL BEAM VERSUS EMPTY BEAM

Magnification is the relative increase in flux as a result of gravitational lensing. There is a subtlety here. One may compare the flux received from the source with the flux received if the universe was entirely homogeneous, in which case the magnification is referred to as the full-beam magnification, μ_{fb} . This is the magnification referred to in Section 2.1. The so-called empty-beam magnification, μ_{eb} , is defined relative to the case where all the matter in the universe is locked up in compact objects, and all lines of sight are empty. As this is the case of minimal magnification (no convergence and assumed negligible shear), then μ_{eb} is always greater than unity. To derive the relationship between the two magnifications, we must compare the solid angles subtended by the source: Ω_{fb} in the full-beam scenario, Ω_{eb} in the empty-beam scenario and Ω_{img} the solid angle of the image observed. Given the conservation of surface brightness, the magnifications are defined by

$$\mu_{\text{fb}} = \frac{\Omega_{\text{img}}}{\Omega_{\text{fb}}} \quad \text{and} \quad \mu_{\text{eb}} = \frac{\Omega_{\text{img}}}{\Omega_{\text{eb}}}. \quad (\text{E1})$$

The solid angles are related to the physical area of the source via the angular diameter distances:

$$\Omega_{\text{fb}}(z) = \frac{A_{\text{src}}}{(1+z)^2 D_{\text{fb}}(z)} \quad (\text{E2})$$

is the appropriate relationship for the full-beam case, and

$$\Omega_{\text{eb}}(z) = \frac{A_{\text{src}}}{(1+z)^2 D_{\text{eb}}(z)} \quad (\text{E3})$$

is appropriate for the empty-beam case. Combining equations (E1), (E2) and (E3), one is easily able to convert between the two:

$$\frac{\mu_{\text{fb}}}{\mu_{\text{eb}}} = \frac{D_{\text{fb}}^2(z)}{D_{\text{eb}}^2(z)}. \quad (\text{E4})$$

The angular diameter distance in the full-beam case, $D_{\text{fb}}(z)$, is equivalent to the Dyer–Roeder distance $D(\tilde{\alpha} = 1; z)$ which is also the FLRW solution:

$$D_{\text{fb}}(z) \equiv \frac{c}{H_0(1+z)} \int_0^z \frac{dz'}{\left[\Omega_{\text{M},0}(1+z')^3 + \Omega_{\Lambda,0} \right]^{1/2}}. \quad (\text{E5})$$

The empty-beam angular diameter distance, $D_{\text{eb}}(z)$, is found by solving the Dyer–Roeder equation for $\tilde{\alpha} = 0$:

$$D_{\text{eb}}(z) \equiv D(\tilde{\alpha} = 0; z) = c \int_0^z \frac{1}{(1+z')^2 H(z')} dz'. \quad (\text{E6})$$

This paper has been typeset from a $\text{TeX}/\text{L}\text{AT}\text{E}\text{X}$ file prepared by the author.